Title
Geometric phase detection via NMR interferometry

Journal
Journal of Magnetic Resonance, 390

ISSN
1090-7807

Authors
Fricke, Sophia N
Reimer, Jeffrey A

Publication Date
2026-09-01

DOI
10.1016/j.jmr.2026.108099

Journal of Magnetic Resonance 390 (2026) 108099

Contents lists available at ScienceDirect

Journal of Magnetic Resonance

journal homepage: www.elsevier.com/locate/jmr

Geometric phase detection via NMR interferometry☆

Sophia N. Fricke [a,*], Jeffrey A. Reimer [b]

[a] Pines Magnetic Resonance Center, University of California, Berkeley, Berkeley, CA 94720, USA
[b] Department of Chemical and Biomolecular Engineering, University of California, Berkeley, Berkeley, CA 94720, USA

ARTICLE INFO

Keywords:
Geometric phase
Holonomy
Berry phase
NMR interferometry
Spinor
Parallel transport

ABSTRACT

We introduce a benchtop NMR method for interferometric detection of geometric phase (also known as Berry/Aharonov–Anandan phase) via spin coherence holonomy in bulk ensembles using phase-wound echo trains. Consecutive π pulses with cyclic phase incrementation drive closed spinor trajectories on the Bloch sphere, while a parity-based analysis isolates the geometric contribution and cancels dynamical offsets by comparing positive and negative winding experiments with a zero-winding reference. The extracted phase increases linearly with echo number, reverses sign under winding reversal, and is independent of echo time in the adiabatic regime, consistent with spinor holonomy arising from parallel transport. Experiments performed in strongly inhomogeneous, low-field conditions demonstrate robustness to B_0 gradients and diffusion. This approach establishes a practical foundation for probing geometric phase effects in NMR, with extensions to non-adiabatic transport, heterogeneous systems, and quantum sensing applications.

1. Introduction

Geometric phase is a fundamental quantum mechanical phenomenon that links the curvature of parameter space to observable physical rotation [1–7]. Although geometric, or Berry/Aharonov–Anandan (AA), phases have been demonstrated in optical and solid-state systems, their direct observation in bulk nuclear spin ensembles has remained underexplored. Conventional nuclear magnetic resonance (NMR) methods are dominated by dynamical phase accumulation and field inhomogeneity, which obscure the geometric contribution [8–11]. A few NMR works have relied upon *interferometric* experiments to demonstrate, for example, the spinor behavior of half-integer spin nuclei [6–8]. Despite early attention to geometric phase in NMR (see, for example, Ref. [12]), systematic experimental approaches in bulk nuclear spin ensembles have remained limited, while geometric and holonomic effects have been actively developed in optical and condensed-matter quantum information platforms.

The unifying structure underlying these phenomena is parallel transport, often introduced in quantum mechanics as the evolution of a state vector constrained to follow a path on the Bloch sphere. More generally, parallel transport is defined through the path-ordered exponential of a connection, $\mathscr{P}\exp\left(-\int_\gamma A\right)$, for the path γ and connection A [13]. Indeed, while the mathematics of parallel transport and geometric phase are well established in differential geometry and gauge theory, they have not historically been emphasized in NMR theory [13–19]. This is not because the underlying physics is absent, but because the standard formalism of NMR was developed around reference frame transformations that remove the most obvious manifestations of geometric transport [20,21]. Ensemble NMR measurements are dominated by dynamical phase accumulation arising from Zeeman evolution, radiofrequency (rf) control fields, and static field inhomogeneity [22,23]. Standard refocusing sequences such as CPMG echo trains are explicitly designed to cancel phase dispersion and retrace spin trajectories, suppressing not only unwanted dephasing but also geometric contributions that depend on directed transport in spin space [24–26]. As a result, geometric phase effects are typically either refocused away by symmetry or absorbed into effective Hamiltonians and phenomenological relaxation terms. Importantly, this limitation does not arise from pulse imperfections or experimental nonidealities, but from the absence of an interferometric symmetry that distinguishes phase contributions by parity under reversal of the spinor path.

From a modern perspective, the rotating frame transformation central to NMR can be understood as a form of gauge fixing on the manifold of spin states [27]. The laboratory-frame Hamiltonian acts as a generator of time evolution from which one may identify a natural connection on

☆ This article is part of a Special issue entitled: 'Low-field magnetic Resonance' published in Journal of Magnetic Resonance.

* Corresponding author.
E-mail address: snfricke@berkeley.edu (S.N. Fricke).

https://doi.org/10.1016/j.jmr.2026.108099
Received 13 January 2026; Received in revised form 22 April 2026; Accepted 29 May 2026
Available online 1 June 2026

projective Hilbert space, governing the parallel transport of spinors in time. Transforming into a rotating frame then corresponds to choosing coordinates that follow this connection exactly, thereby eliminating rapid precession by construction. In doing so, curvature associated with transport becomes hidden: evolution appears locally flat, with residual effects interpreted as control fields or detuning. Because NMR theory emphasizes toggling frames, interaction frames, and average Hamiltonian theory, each involving successive changes of reference frame, geometric transport is rarely made explicit. As a result, quantities that depend on comparing different paths, such as holonomy or curvature-induced phase shifts, are typically folded into effective Hamiltonians rather than isolated as geometric observables.

The absence of explicit parallel transport language in NMR should therefore be seen as historical and methodological rather than fundamental. When experiments depart from these regimes – for example, through time-dependent quantization axes or deliberately non-commuting pulse sequences – the underlying geometric structure becomes relevant. In this regime, parallel transport provides a natural organizing principle because it distinguishes between phase accrued due to the local generator and phase accrued due to the geometry of the path itself. We now show how parallel transport can be made explicit in bulk NMR by engineering directed spinor loops within a refocusing echo train.

Here we introduce a benchtop NMR interferometric method that isolates geometric (Berry/Aharonov–Anandan) phase in spin coherences through consecutive π-pulse phase winding within an echo train. By recording echo trains with positive, negative, and zero winding and analyzing their parity, dynamical phase contributions are cancelled while the odd-in-winding geometric phase is preserved. The resulting phase increases linearly with echo number, characteristic of holonomy arising from parallel transport on the Bloch sphere. Crucially, the interferometric element of this approach does not rely on resolving superpositions of distinct spinor eigenstates, but on comparing the accumulated phase associated with distinct paths through control space. Interferometry here is implemented by path parity rather than state selectivity. Geometric phase detection in this context does not require resolving relative phase differences between $|+\rangle$ and $|-\rangle$ spinor states; it is sufficient that a spinor vector undergoes parallel transport through a sequence of non-commuting rotations with the accumulated holonomy measured relative to a fixed reference phase, here defined by the receiver. This approach enables measurements in inhomogeneous, low-field environments appropriate for quantum sensing, remote environments, and education.

2. Results

Consecutive π-pulse phase winding in an echo train forms a spinor interferometer that is inherently self-referencing (Fig. 1). Taking the half-difference of positive and negative windings referenced to a zero-winding experiment isolates the odd-in-winding Berry/AA phase associated with transverse coherences. This analysis cancels B_0 drift, receiver phase, and other dynamical offsets to first order, enabling robust geometric phase detection without requiring homogeneous fields or high-resolution conditions.

The protocol consists of three echo trains: positive winding, negative winding, and zero winding. Their combined analysis isolates the geometric component. In general, the net propagator per cycle can be written

$$U_{\pm} \sim e^{i\left(\varphi_{\rm dyn} \pm \varphi_{\rm geo}\right)}, \tag{1}$$

where φ_{geo} is the geometric (Berry/AA) phase that changes sign when winding is reversed, and φ_{dyn} contains ordinary dynamical phase (off-resonance effects, small timing asymmetries, etc.). By recording three echo trains with positive, negative, and zero winding, the geometric phase of coherence states can be directly extracted with maximal

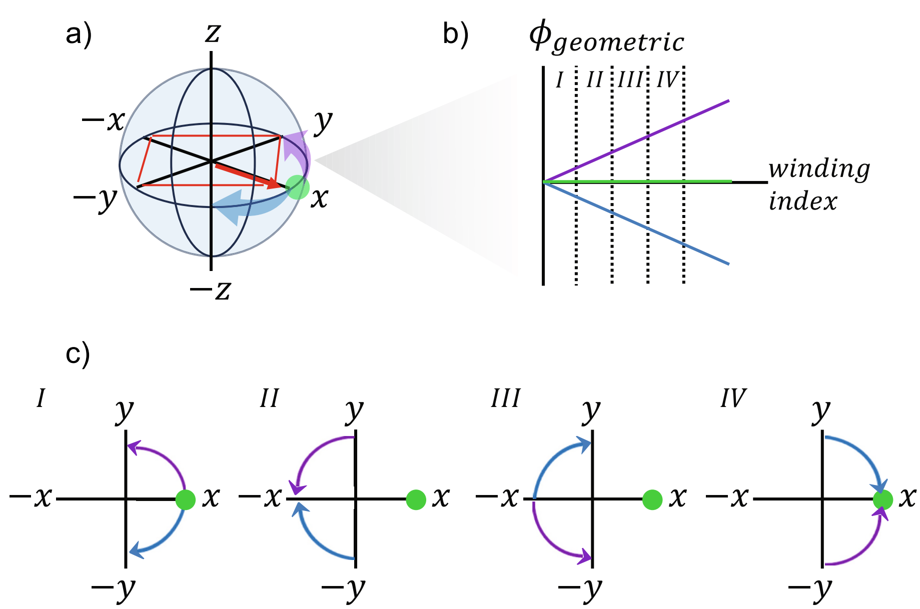

Fig. 1. Schematic of how phase-winding NMR interferometry isolates geometric phase from dynamical transverse evolution of coherence states through parity, revealing linear spinor holonomy. Positive winding around the transverse plane of the Bloch sphere is shown in purple (a), corresponding to geometric phase that increases linearly with winding index (b). Negative winding is shown in blue (a), corresponding to geometric phase that decreases linearly with winding index (b). A zero-winding reference (green) does not undergo directed transport around the Bloch sphere (a) and hence accumulates no geometric phase (b). (c) Here the π pulse phase-increments by 90° in the transverse plane for each consecutive echo in a single scan, i.e., for a 3200-echo CPMG, the π pulses loop through this cycle 800 times within each scan (see Methods for the pulse sequence, depicted in the Graphical Abstract). Each sub-panel shows the transverse plane and the π-pulse rotation applied at that step, with purple arrows tracing positive winding and blue arrows tracing negative winding. Over the four steps (I, II, III, IV), the spinor is parallel transported around the transverse circle, returning to +x after each full cycle. The dashed vertical lines in (b) mark the four sub-steps and align with (c), illustrating the correspondence between pulse step and accumulated geometric phase. (For interpretation of the references to colour in this figure legend, the reader is referred to the web version of this article.)

sensitivity by taking the half-difference of the complex echo decays,

$$\varphi_{geo}(n) \approx \frac{1}{2}(\arg S_{+}(n) - \arg S_{-}(n)) \tag{2}$$

where $S_{\pm}(n)$ is the complex echo amplitude recorded at echo index n for echo trains with $\pm$ winding. Given $S_{\pm} = |S_{\pm}|e^{i\theta}$ and $\theta = arctan(\mathrm{Im}/\mathrm{Re})$, the term $\arg S_{\pm}(n)$ is the phase of the n^{th} echo under $\pm$ winding. To remove residual dynamical contributions, the half-difference is referenced to a zero-winding experiment:

$$\varphi_{geo}(n) \approx \frac{1}{2}\left[\arg\left(\frac{S_{+}(n)}{S_{0}(n)}\right) - \arg\left(\frac{S_{-}(n)}{S_{0}(n)}\right)\right]. \tag{3}$$

This normalized difference cancels receiver phase, B_0 drift, and other dynamical phase terms to first order, rendering the analysis robust in inhomogeneous and low-field environments. Relaxation and diffusive attenuation affect only the signal magnitude, not the odd-in-winding geometric phase. Each 2π phase cycle (here every four echoes with $\pi/2$ phase incrementation) traces a closed path on the Bloch sphere, set by the π-pulse winding. Each pulse contributes a fixed Berry phase increment per echo, $\Delta\varphi_{geo}$, if the receiver phase remains fixed. Over n echoes, the total geometric phase is approximately

$$\varphi_{geo}(n) \approx n\Delta\varphi_{geo}. \tag{4}$$

Plotting the extracted $\varphi_{geo}(n)$ versus echo index n yields a straight line through the origin, to which a linear fit reports the geometric phase per echo cycle as the slope. The sign of this slope reverses between positive and negative winding, while referencing to the zero-winding experiment (or the first echo) yields a near-zero intercept. This linear dependence of $\varphi_{geo}(n)$ is observed experimentally in Fig. 2, where the slope directly reports the geometric phase increment per pulse.

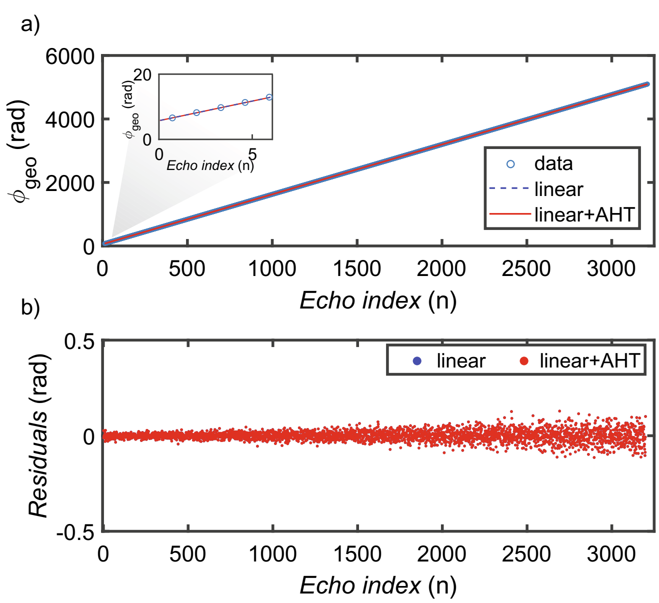

Fig. 2. Exemplary [1]H geometric phase data of (a) water and (b) residuals extracted according to Eq. (3) from an echo train of 3200 echoes with a 75 μs echo time using a 4-step phase winding. A linear fit based on Eq. (4) yields the expected geometric phase incrementation of 1.5708 rad≈$\pi/2$ per echo. Including additional 2nd order average Hamiltonian terms from Eq. (20) quantifies the effect of diffusion in a constant magnetic field gradient by modelling the cross commutators as linear combinations of sines and cosines with pulse-synchronized periodicity (modulo 4 greater than geometric phase winding frequency), which is found to be statistically negligible (0.0007±0.0007 rad). An F-test for fit comparison yields $F = 0.46$ ($p = 0.631$). Akaike information criteria (AIC) show no improvement in fit (linear AIC$= -$ 23,084.2) with the inclusion of 2nd order AHT terms (AIC$= -$ 23,081.1 with 2nd order AHT terms).

Relaxation and diffusion attenuate the magnitude $|S|$ but do not affect the geometric phase (slope) unless phase noise dominates at low signal-to-noise ratios in later echoes; truncating the echo train before this point preserves the fidelity of the linear geometric phase evolution in Eq. (4). To formalize the odd-in-winding geometric phase extraction, we consider the per-cycle propagator and its decomposition into geometric and dynamical contributions.

Any systematic deviation from this behavior in $\varphi_{geo}(n)$ would indicate residual dynamical offsets (B_0 drift, pulse miscalibration, or eddy currents) or non-adiabatic effects (vide infra). Taking the $\pm$ half-difference provides the most robust suppression of such offsets because it removes the vast majority of dynamic phase influence while preserving the odd-in-winding geometric phase ramp. Consistent with this expectation, diffusion in an inhomogeneous magnetic field is modeled using second-order average Hamiltonian theory and found to be statistically negligible (Fig. 2). By the same parity argument, any spatial variation in the gradient strength across the sensitive slice enters only through even-in-winding dynamical terms and is likewise suppressed in the $\pm$ half-difference.

In purely adiabatic evolution, individual eigenkets evolve with no transitions to other states [4]. Here, the relevant eigenkets are superposition states generated by an initial $\pi/2$ pulse, followed by a series of π pulses whose phases increment in a four-step repeating loop. Each echo cycle traces a closed trajectory on the Bloch sphere. When the winding is well-defined, the geometric phase increment per pulse is fixed, yielding a linear dependence of $\varphi_{\text{geo}}(n)$ with slope equal to the constant Berry phase increment per pulse. Crucially, the effect is purely path-dependent rather than rate-dependent: its magnitude is independent of echo time because it arises solely from repeating the same cyclic path.

Echo-time dependence of the measured geometric phase would therefore signal coupling between rf-driven evolution and spin dynamics in an inhomogeneous field. When the gradient evolution angle per cycle varies with echo time, the dynamical phase term $\Delta\varphi_{\text{dyn}}$ becomes coupled to stochastic motion such as molecular diffusion or velocity autocorrelation [28–30]. In contrast, the geometric component remains defined by the closed spinor path in Hilbert space and, if truly adiabatic, is independent of path speed. For each echo time, $\varphi_{\text{geo}}(n)$ must then be extracted from the $\pm$ winding difference. If cancellation is ideal, the computed slope remains constant until the noise floor limit, beyond which deviations from linearity appear (Fig. 3). In practice, weak echo-time dependence may arise from non-adiabaticity, eddy currents, or diffusion-induced dephasing.

The observations and methods described above do not invoke new physical principles or new forms of NMR spectroscopy. Instead, they

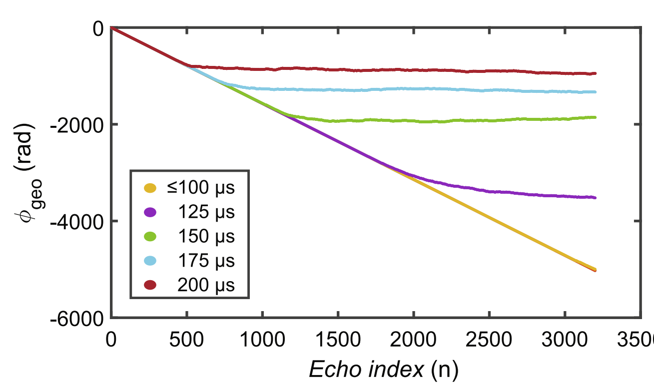

Fig. 3. Echo time dependence of the measured geometric phase for water with echo times of 55, 75, 100, 125, 150, 175, and 200 μs (legend) using a 4-step phase winding of $-\pi/2$. Data from the shortest three echo times are statistically equivalent and appear overlaid (yellow). All other traces show linear accumulation of geometric phase until the signal decays when signal-to-noise drops and only noise remains. (For interpretation of the references to colour in this figure legend, the reader is referred to the web version of this article.)

recast familiar NMR pulse sequences in the language of holonomy, making explicit the geometric structure implicit in standard spin manipulations and enabling geometric phase to be exploited in new contexts. Toward that end, we now connect the observed phase evolution to its description within quantum geometric phase theory.

3. Geometric phase theory

To connect the observed phase evolution to underlying quantum geometry, we begin by recalling the gauge potential formalism for Berry and Aharonov–Anandan geometric phases. If echo time dependence persists and cannot be attributed to dynamical contamination (relaxation or diffusive attenuation) or imperfect cancellation, it may indicate a genuine coupling between stochastic motion and the spinor path. Such coupling would link geometric phase to classical transport and entropy, revealing how geometric phase persists, distorts, or cancels as spins undergo stochastic motion at different time scales. Moving toward path rate-resolved detection thus transforms this static proof-of-principle into an experimental framework for probing the interaction between geometric phase, diffusion, and entropy evolution. To enter this regime, a non-adiabatic generalization of geometric phase must be established.

3.1. Aharonov–Anandan geometric phase

The Aharonov–Anandan (AA) geometric phase is the non-adiabatic generalization of the Berry phase [2]. For a cyclic evolution of a quantum state, $|\psi(t)\rangle = e^{i\alpha}|\psi(0)\rangle$, the accumulated geometric phase over time T is

$$\varphi_{AA} = \alpha - \frac{1}{\hbar}\int_0^T \langle \psi(t)\,|H(t)\,\psi(t)\,\rangle dt$$
$$= arg\langle \psi(0)\,|\psi(T)\,\rangle - Im\int_0^T \left\langle \psi(t)\,|\frac{\partial \psi(t)}{\partial t}\right\rangle dt. \tag{5}$$

In the adiabatic limit, this reduces to Berry phase. In the present experiments, the cyclic evolution corresponds to one complete phase-winding cycle of the refocusing pulse train, such that the accumulated AA phase manifests directly as a systematic phase shift of successive echoes. Practically, the ± winding half-difference analysis continues to isolate the geometric contribution even when the loop is not strictly adiabatic, underscoring the robustness of the interferometric approach.

3.2. Gauge potential and geometric Hamiltonian

Fundamentally, geometric phase arises from a gauge structure that can be represented in the Hamiltonian

$$H_{geo}(t) = \hbar\frac{\partial\lambda}{\partial t}\cdot\boldsymbol{A}_\lambda \tag{6}$$

where $\boldsymbol{A}_\lambda$ is a gauge vector potential defined by

$$\boldsymbol{A}_\lambda \equiv -iU_{rf}^{\dagger}\frac{\partial U_{rf}}{\partial\lambda}, \tag{7}$$

with λ a coordinate on the parameter manifold that defines the spinor path. In NMR, this gauge term arises naturally from the time dependence of the rf rotation axis; its integral over one winding cycle corresponds to the experimentally observed geometric phase increment per echo. For spin-½, the matrix-valued connection of Eq. (7) can be expanded on the SU(2) generators as $-iU_{rf}^{\dagger}\dot{U}_{rf} = \boldsymbol{a}(t)\cdot\boldsymbol{S}$, with $\boldsymbol{a}(t)$ the generator coefficients, such that $H_{geo}(t) = \hbar\boldsymbol{a}(t)\cdot\boldsymbol{S}$. More generally, phase in NMR is associated with gradients in electromagnetic gauge fields imposed by B_0 or B_1 fields [13]. Projecting $\boldsymbol{A}_\lambda$ onto a locally followed eigenstate maps this term to an experimental observable; its time integral yields the geometric phase.

3.3. Parity under winding reversal

For spin-½ operators with SU(2) symmetry, successive rotations about non-commuting axes generate an effective rotation proportional to the enclosed solid angle on the Bloch sphere. As the rf phase winds cyclically, the sequence of rotation axes traces a closed loop; the accumulated commutator $[\boldsymbol{S}\cdot\hat{\boldsymbol{n}}_1, \boldsymbol{S}\cdot\hat{\boldsymbol{n}}_2] = i\boldsymbol{S}\cdot(\hat{\boldsymbol{n}}_1\times\hat{\boldsymbol{n}}_2)$, with unit axes denoted $\hat{\boldsymbol{n}}$, produces an additional rotation whose angle equals the solid angle enclosed by this path. For a spin-½ aligned with the loop, the resulting geometric phase per cycle is

$$\varphi_{\rm geo} = -m_s\Omega, \tag{8a}$$

which is the Berry or, more generally, the AA phase for a pure eigenstate $|m_s\rangle$ traversing a loop enclosing solid angle Ω. [31–34] In bulk NMR, however, the detected phase is tied to spin coherences arising from off-diagonal density matrix elements $\rho_{m_s m_s'}$ that acquire the geometric phase difference

$$\varphi_{m_s m_s'} = \varphi_{m_s} - \varphi_{m_s'} = -\left(m_s - m_s'\right)\Omega. \tag{8b}$$

For $m_s = \pm\frac{1}{2}$, single-quantum coherences are $\left(m_s - m_s'\right) = 1$ and $\varphi_{m_s m_s'} = -\Omega$, consistent with the experimentally extracted phase increment per winding cycle ($-\Omega$ per closed 2π loop, equivalent to $-\pi/2$ increment per echo in the four-step winding used here). Further derivation is provided in Appendix A.

With U(1) gauge structure, the connection $\boldsymbol{A}_\lambda = i\langle n(\lambda)\,|\partial_\lambda n(\lambda)\,\rangle$ acts as vector potential in control parameter space, and the curvature $\boldsymbol{F}_{\lambda\lambda'} = \partial_\lambda\boldsymbol{A}_{\lambda'} - \partial_{\lambda'}\boldsymbol{A}_\lambda$ corresponds to the associated magnetic field [13,35].[1] Here λ and λ' label coordinates on the control manifold (e.g., $\lambda = \theta$, $\lambda' = \varphi$ for the Bloch sphere). The geometric phase represents the holonomy acquired by parallel transport along a closed path,

$$\varphi_{\rm geo} = \oint \boldsymbol{A}_\lambda d\lambda = \iint \boldsymbol{F} d\boldsymbol{S} \tag{9}$$

where, by Stokes' theorem, the line integral of the gauge potential around the closed path is equivalent to the surface integral of its curvature over the enclosed area. Both are gauge-invariant modulo 2π. Here, λ denotes the rf phase, so ± winding reverses the loop orientation from $\varphi_{\rm geo}\rightarrow -\varphi_{\rm geo}$.

3.4. Average Hamiltonian analysis in a constant gradient

To determine whether static gradients or finite pulse durations can introduce spurious odd-in-winding contributions that mimic geometric phase, we analyze a single winding cycle using Average Hamiltonian theory (AHT). [36] When signals from positive and negative windings are collected and their half-difference is taken, any quantity X is projected onto its parity under winding reversal: $X_{\rm odd} = \frac{1}{2}\left(X^{(+)} - X^{(-)}\right)$, $X_{\rm even} = \frac{1}{2}\left(X^{(+)} + X^{(-)}\right)$. The odd component survives in the ± difference, whereas the even component cancels. The geometric term is odd under winding reversal, while most ordinary dynamical terms from a constant gradient are even. To evaluate one cycle via a Magnus expansion with rf winding in a constant gradient, we start from the laboratory frame Hamiltonian

[1] More generally, for a matrix-valued gauge connection the curvature is given in component form by $F_{\lambda\lambda'} = \partial_\lambda A_{\lambda'} - \partial_{\lambda'}A_\lambda + [A_\lambda, A_{\lambda'}]$, or, in exterior calculus form, $F = \mathbf{d}A + A\wedge A$. [13] In the present case, where the Berry connection is projected onto a single instantaneous eigenstate, the connection is Abelian and the commutator term vanishes. This reduction mirrors electromagnetism, where the U(1) gauge field is Abelian and $[A_\lambda, A_{\lambda'}] = 0$. For non-Abelian gauge fields or degenerate subspaces, however, the commutator term plays an essential role. [35]

$$H(t) = H_{\mathrm{rf}}(t) + H_g, \tag{10}$$

where $H_{\mathrm{rf}}(t)$ is the time-dependent rf component. The static term arising from a constant field gradient is

$$H_g = \hbar\,\omega_g(\boldsymbol{r})\,S_z, \tag{11}$$

with $\omega_g(\boldsymbol{r}) = \gamma \boldsymbol{G} \bullet \boldsymbol{r} = \gamma G z$. Transforming into the rf-fixed toggling frame, the propagator is

$$U_{rf}(t) = \mathscr{T}\exp\left[-\frac{i}{\hbar}\int^{t} H_{rf}(s)ds\right] \tag{12}$$

and the effective Hamiltonian becomes

$$\widetilde{H}(t) = U_{rf}^{\dagger}H_g U_{rf} - i\hbar U_{rf}^{\dagger}\frac{\partial U_{rf}}{\partial t} \equiv \widetilde{H}_g(t) + H_{geo}(t) \tag{13}$$

where $\widetilde{H}_g(t)$ captures the gradient term in toggling frame and $H_{geo}(t)$ is the geometric (gauge) contribution. Writing these two components explicitly yields

$$\widetilde{H}_g(t) = \hbar\omega_g(\boldsymbol{r})\boldsymbol{S}\cdot\widehat{\boldsymbol{n}}_z(t) \tag{14}$$

where $\widehat{\boldsymbol{n}}_z(t) = U_{rf}^{\dagger}\widehat{\boldsymbol{z}}U_{rf}$ is the instantaneous direction to which S_z is rotated by the pulse train. Between ideal, instantaneous π pulses, $\widehat{\boldsymbol{n}}_z(t) \rightarrow \pm\widehat{\boldsymbol{z}}$, reducing to the familiar toggling function $f(t) = \pm 1$, such that

$$\widetilde{H}_g(t) = \hbar\omega_g f(t) S_z. \tag{15}$$

Considering the geometric part of the toggling frame Hamiltonian, we have

$$H_{geo}(t) = -i\hbar U_{rf}^{\dagger}\frac{\partial U_{rf}}{\partial t} \equiv \hbar\boldsymbol{a}(t)\cdot\boldsymbol{S} \tag{16}$$

which is the adiabatic gauge potential responsible for the accumulated Berry/AA geometric phase. Under winding reversal, $\boldsymbol{a}(t) \rightarrow -\boldsymbol{a}(t)$, corresponding to a reversal of the loop direction on the Bloch sphere. Evaluating one complete cycle T with a Magnus expansion yields

$$U(T) = \exp\left[-\frac{i}{\hbar}(\Omega_1 + \Omega_2 + \ldots)\right]. \tag{17}$$

The first order average Hamiltonian is

$$\Omega_1 = \int_0^T \widetilde{H}(t)dt = \hbar\boldsymbol{S}\cdot\left[\int_0^T \boldsymbol{a}(t)dt + \omega_g\int_0^T f(t)\widehat{\boldsymbol{z}}dt\right]. \tag{18}$$

The first term, containing the integral over $\boldsymbol{a}(t)$, gives rise to the geometric phase. It is odd under winding reversal because it originates at zero accumulated phase and changes sign when the winding sense is inverted. The second term represents the dynamical phase accumulated from the constant gradient during the echo train; this contribution is even in winding. The square wave modulation $f(t)$ integrates to zero over a full echo cycle, so to first order this term vanishes. Because it is even, it also cancels in the $\pm$ half-difference, leaving Ω_1 contributing solely to the odd (geometric) phase component. The first-order cancellation of gradient-induced phase explains the near-zero intercept and high linearity of the data in Fig. 2.

The second order average Hamiltonian involves evaluating the commutator

$$\Omega_2 = \frac{1}{2}\int_{t_2<t_1}\left[\widetilde{H}(t_1), \widetilde{H}(t_2)\right]dt_1 dt_2. \tag{19}$$

Inserting the terms for gradient (dynamical phase) and geometric components of $\widetilde{H}(t)$ (gives)

$$\Omega_2 = \frac{1}{2}\iint\left(\left[\widetilde{H}_g(t_1), \widetilde{H}_g(t_2)\right] + \left[H_{geo}(t_1), H_{geo}(t_2)\right] + \left[\widetilde{H}_g(t_1), H_{geo}(t_2)\right] + \left[H_{geo}(t_1), \widetilde{H}_g(t_2)\right]\right)dt_1 dt_2. \tag{20}$$

The first commutator, $\left[\widetilde{H}_g(t_1), \widetilde{H}_g(t_2)\right]$, is proportional to $[\boldsymbol{S}\cdot\widehat{\boldsymbol{n}}_z(t_1), \boldsymbol{S}\cdot\widehat{\boldsymbol{n}}_z(t_2)]$. For ideal, instantaneous pulses, the effective axis remains $\pm\widehat{\boldsymbol{z}}$ between pulses, so $[S_z, S_z] = 0$. With finite pulses, however, $\widehat{\boldsymbol{n}}_z(t)$ actively rotates during the pulse, giving $[\boldsymbol{S}\cdot\widehat{\boldsymbol{n}}_z(t_1), \boldsymbol{S}\cdot\widehat{\boldsymbol{n}}_z(t_2)] \neq 0$ and producing an extra rotation proportional to $\boldsymbol{S}\cdot(\widehat{\boldsymbol{n}}_z(t_1) \times \widehat{\boldsymbol{n}}_z(t_2))$. This term is even in winding if the pulse shapes are identical for the $\pm$ experiments and therefore cancels in the half-difference analysis.

The second commutator, $[H_{geo}(t_1), H_{geo}(t_2)]$, represents the non-Abelian contribution whose integrated effect reproduces the geometric curvature corresponding to the solid angle traversed by the spinor. This term is odd under winding reversal.

3.5. Finite pulse width effects and cross-commutators

The cross commutators, $\left[\widetilde{H}_g(t_1), H_{geo}(t_2)\right]$ and $\left[H_{geo}(t_1), \widetilde{H}_g(t_2)\right]$, generate an additional term written as $[\boldsymbol{a}(t_1)\cdot\boldsymbol{S}, \omega_g f(t_2)S_z] = i\hbar\omega_g f(t_2)\boldsymbol{S}\cdot(\boldsymbol{a}(t_1) \times \widehat{\boldsymbol{z}})$. Upon double integration, this yields an extra rotation proportional to ω_g and to the time-integrated geometric path. Because $\boldsymbol{a}(t) \rightarrow -\boldsymbol{a}(t)$ under winding reversal while $f(t)$ remains unchanged, these cross terms are odd and therefore survive in the $\pm$ half-difference. Their amplitude scales approximately as the product of $\omega_g\tau_p$ and the geometric loop area. This provides the formal route through which a constant gradient can couple into the geometric component when pulses have finite duration.

Overall, in the instantaneous δ-pulse limit, the constant gradient contributes neither to Ω_1 (zero time average) nor to Ω_2 through $\left[\widetilde{H}_g, \widetilde{H}_g\right]$; only the geometric term remains by parity. Finite pulse duration in a static gradient, however, introduces odd cross-commutator terms $\left[\widetilde{H}_g, H_{geo}\right]$ that scale as $\omega_g\tau_p$ times the geometric loop area, producing a small but quantifiable bias, where τ_p denotes pulse width. A quantitative estimate using experimental parameters confirms that diffusion during an echo cycle is negligible. Even though diffusion is negligible between pulses, finite pulse duration in a strong static gradient can generate cross-commutator terms that weakly bias the geometric phase slope (see Methods).

3.6. Discussion and interpretation

To summarize: at first order, the gradient modulation cancels because the toggling function $f(t)$ alternates sign between free evolution intervals, giving a zero net $\int f(t)dt$ per echo. At second order, however, the odd cross commutator terms generated during finite pulses – when the rotation axis sweeps – do not cancel. This effect is analogous to CRAZED-style mixing, in which gradients combined with non-commuting rotations introduce additional phase factors that can mimic geometric winding and bias the measured slope. [37] Fortuitously, the periodicity of this term (one oscillation per pulse) is distinct from the four-pulse geometric phase incrementation. Including this term in the fitting model allows quantitative, statistical assessment of its magnitude.

Together, this analysis shows that the observed geometric phase accumulation is symmetry-protected by parity under winding reversal and is robust against static field gradients and diffusion to first order. Finite pulse duration introduces higher-order corrections whose magnitude and scaling are predictable and experimentally distinguishable. As a result, the linear geometric phase ramps observed in Figs. 2 and 3 can be directly interpreted as holonomy arising from parallel transport of spinors in projective Hilbert space. The present low-field implementation was chosen to demonstrate robustness in strongly inhomogeneous environments, but the interferometric protocol is not restricted to low fields; extensions to high fields and to conventional spectroscopic pulse sequences remain to be explored.

4. Conclusions

We have demonstrated a benchtop NMR approach for detecting geometric (Berry/Aharonov–Anandan) phase using consecutive π-pulse phase incrementation within an echo train. Phase winding drives a closed spinor trajectory on the Bloch sphere each cycle, producing an odd-in-winding geometric phase distinct from ordinary dynamical offsets. By recording echo trains with positive, negative, and zero winding, the geometric phase is extracted through a half-difference analysis of the complex echo decays, canceling B_0 drift, receiver phase, and other dynamical contributions to first order.

The resulting phase accumulates linearly with echo number and reverses sign under winding reversal, providing an unambiguous interferometric signature of geometric phase. Comparison across echo times confirms the expected adiabatic invariance of the geometric contribution, while second-order AHT analysis quantifies small cross-terms arising from finite pulse width in static magnetic field gradients.

These results establish a robust and general route for interferometric detection of geometric phase in bulk spin ensembles using standard low-field NMR hardware and pulse sequences. In contrast to interferometric geometric phase measurements that rely on three-level systems to provide an internal phase reference, here the role of the third level is played by the receiver, which enables geometric phase detection in a two-level spin system and substantially broadens accessibility. Beyond serving as a proof-of-principle, this framework provides a foundation for exploring how quantum geometric phase couples to diffusion, irreversible entropy production, and transport in experimentally relevant, inhomogeneous environments. More broadly, this work portends reintegration of geometric phase in NMR as a tool for exploring parallel transport and holonomy in quantum spin systems.

5. Methods

NMR echo train [30,38] measurements were performed at room temperature with an NMR-MOUSE (Mobile Universal Surface Explorer) PM25 0.3 T unilateral magnet [39,40] and a Magritek Kea II spectrometer at a ^{1}H resonant frequency of 13.11 MHz with a constant gradient along the z-axis of 7 T m^{-1}, using Prospa v3.61 software from Magritek (Malvern, PA). For all experiments, the number of π rf pulses in a Carr–Purcell–Meiboom–Gill pulse sequence (CPMG) [25,26] was 3200, π/2 rf pulse lengths were 2.5 μs, the delay between π rf pulses was varied between 55 and 200 μs, and the repetition time for signal averaging was 9.5 s to sum 128 CPMG transient signals. Experiments were recorded in triplicate to report the statistical average and standard error.

5.1. Effects of finite pulse duration in a strong static gradient

On a unilateral magnet such as the NMR-MOUSE, there is a constant gradient, $G_z = 7\,\mathrm{T\,m^{-1}}$. [39,40] A short echo time of 75 μs is chosen so that the toggling function $f(t) = \pm 1$ averages to zero over a full echo, giving $\Omega_{1,grad} = 0$. For a sample of free water with self-diffusion coefficient $D \approx 2.3 \times 10^{-9}\,\mathrm{m^2 s^{-1}}$, the one-dimensional diffusion step over 100 μs is $\sigma_{1D} \approx \sqrt{2D\Delta t} \approx \sqrt{2 \cdot 2.3 \times 10^{-9} \cdot 10^{-4}} \approx 0.68\,\mu\mathrm{m}$, i.e., <1 μm per interval. With an appropriate excitation bandwidth, this motion is negligible for toggling-function averaging.

To compare the pulse bandwidth versus the gradient, a $\tau_{90} = 2.5\,\mu s$ hard pulse has a bandwidth of $\sim 1/\tau_{90} \approx 400$ kHz. The spatial frequency sweep of the gradient is $\gamma G \approx (42.58\text{ MHz T}^{-1})(7\text{ T m}^{-1}) \approx 298$ MHz m$^{-1} \approx 298$ Hz μm^{-1}. A 400 kHz pulse bandwidth therefore corresponds to an excited slice thickness of $\Delta z \approx \text{bandwidth}/(\gamma G) \approx 1.3$ mm. This thickness is much larger than the ~1 μm diffusion range, confirming that diffusion does not compromise the first order cancellation of the toggling function. While this is advantageous for refocusing between pulses, it also implies that during each pulse, the spins across the excited slice experience significant off-resonance offsets from the gradient. For a $\tau_{180} \approx 5\,\mu s$ pulse, the dimensionless parameter $\Delta\omega_g \tau_p$ across a 1 mm slice can approach unity, indicating that the cross-commutator term may not be negligible.

5.2. Pulse sequence phase incrementation

To perform geometric phase winding, consecutive π pulses in each transient echo train were phase-incremented in four steps of π/2: i.e., [x, y, −x, −y] and [x, −y, −x, y] for positive and negative winding. The interferometric approach requires three experiments, for example:

1. Positive phase winding: initial π/2 pulse = x; π = [y,−x,−y,x] repeated *n* echoes/4; receiver = x.

Here the π pulse phase-increments for each consecutive echo in a single scan, i.e., for a 3200-echo CPMG, the π pulses loop through this cycle 800 times within each scan.

2. Negative phase winding: initial π/2 pulse = x; π = [y,x,−y,−x] repeated *n* echoes/4; receiver = x.

3. Zero phase winding: initial π/2 pulse = x; π = [y,y,y,y] repeated *n* echoes/4; receiver = x.

This acts as a control and as a reference to subtract from positive or negative phase winding experiments.

To cancel artifacts arising from pulse imperfections, the initial π/2 rf pulse and the receiver were cycled between + x and − x phase, while holding the π rf pulse phase constant at + y for zero-winding reference experiments. To maintain continuity in the direction of geometric phase winding across scans (so geometric phase adds constructively rather than cancels), the phase of the first π pulse must alternate sign depending on the π/2 pulse phase. Thus, the three experiments become:

1. Positive phase winding:

Initial π/2 pulse = x; π = [y, −x, −y, x] repeated *n* echoes/4; receiver = x.

Initial π/2 pulse = −x; π = [−y, x, y, −x] repeated *n* echoes/4; receiver = −x.

This ensures the positive phase winding accumulates rather than canceling out. Likewise for the others:

2. Negative phase winding:

Initial π/2 pulse = x; π = [y, x, −y, −x] repeated *n* echoes/4; receiver = x.

Initial π/2 pulse = −x; π = [−y, −x, y, x] repeated *n* echoes/4; receiver = −x.

3. Zero phase winding:

Initial π/2 pulse = x; π = [y, y, y, y] repeated *n* echoes/4; receiver = x.

Initial π/2 pulse = −x; π = [−y, −y, −y, −y] repeated *n* echoes/4; receiver = −x.

This acts as a control and as a reference to subtract from positive or negative phase winding experiments.

All data analysis was accomplished with MATLAB (Mathworks, Natick, MA). An exemplary script is provided below that can be saved as an m file for analysis.

5.3. Exemplary script

```
function out = berry(Splus, Sminus, Szero, label)
% Inputs: [N x 3] arrays [time, real, imag] for +, -, 0 winding
% Fits geometric phase per echo (slope) plus optional period-4 oscillatory
% offset from 2nd order average Hamiltonian theory cross-terms
% Reports slope, 2nd order offset (AHT), SEs, and model comparison (F-test, AIC)

    % --- Build complex arrays ---

Sp = complex(Splus(:,2),  Splus(:,3));
Sm = complex(Sminus(:,2), Sminus(:,3));
Sz = complex(Szero(:,2),  Szero(:,3));

tiny = 1e-30; Sz(abs(Sz)==0)=tiny;
Rplus  = Sp ./ Sz;
Rminus = Sm ./ Sz;

phi_geo = 0.5*( unwrap(angle(Rplus)) - unwrap(angle(Rminus)) );
N = numel(phi_geo);
n = (1:N).';

% ===========================
% Linear + AHT period-4 model
% phi(n) = a0 + b*n + C4*sin(pi/2*n) + D4*cos(pi/2*n)
% ===========================
w4 = pi/2;
X_full = [ones(N,1), n, sin(w4*n), cos(w4*n)];
beta_full = X_full \ phi_geo;
yfit_full = X_full*beta_full;
resid_full = phi_geo - yfit_full;
p_full = size(X_full,2);
dof_full = N - p_full;
SSR_full = resid_full.'*resid_full;

% Parameters
a0 = beta_full(1);
slope = beta_full(2);
C4 = beta_full(3); D4 = beta_full(4);
ripple_amp = hypot(C4,D4);
ripple_phase = atan2(D4,C4);

% Covariance and standard error
sigma2_full = SSR_full/dof_full;
Cbeta = sigma2_full*inv(X_full.'*X_full); %#ok<MINV>
se_full = sqrt(diag(Cbeta));
slope_se = se_full(2);
C4_se = se_full(3); D4_se = se_full(4);
if ripple_amp>0
    ripple_amp_se = sqrt((C4/ripple_amp)^2*C4_se^2 + (D4/ripple_amp)^2*D4_se^2);
else
    ripple_amp_se = sqrt(C4_se^2 + D4_se^2);
end

% ===========================
% Slope-only model
% ===========================
X_lin = [ones(N,1), n];
beta_lin = X_lin \ phi_geo;
yfit_lin = X_lin*beta_lin;
resid_lin = phi_geo - yfit_lin;
p_lin = size(X_lin,2);
dof_lin = N - p_lin;
SSR_lin = resid_lin.'*resid_lin;
slope_only = beta_lin(2);
sigma2_lin = SSR_lin/dof_lin;
Sxx = sum((n-mean(n)).^2);
slope_only_se = sqrt(sigma2_lin / Sxx);

% ===========================
% Model comparison
% ===========================
% F-test: does adding 2nd order AHT terms to fit significantly reduce SSR?
F = ((SSR_lin - SSR_full)/(p_full-p_lin)) / (SSR_full/dof_full);
pval = 1 - fcdf(F, p_full-p_lin, dof_full);

% AIC
AIC_lin  = N*log(SSR_lin/N)  + 2*p_lin;
AIC_full = N*log(SSR_full/N) + 2*p_full;
```

```
    % --- Plot
    figure('Color','w');
    subplot(2,1,1);
    plot(n, phi_geo, 'o', 'MarkerSize', 3); hold on;
    plot(n, yfit_lin, 'b--', 'LineWidth', 1.2);
    plot(n, yfit_full,'r-',  'LineWidth', 1.2);
    xlabel('Echo index (n)'); ylabel('\phi_{geo} (rad)');
    legend('data','linear','linear+AHT','Location','best');
    ttl = sprintf('%s | slope = %.4f±%.4f rad/echo; ripple = %.4f±%.4f rad\nF=%.2f (p=%.3f), AIC_lin=%.1f,
AIC_full=%.1f',...
        label, slope, slope_se, ripple_amp, ripple_amp_se, F, pval, AIC_lin, AIC_full);
    title(ttl,'Interpreter','tex');

    subplot(2,1,2);
    plot(n, resid_lin, 'b.'); hold on;
    plot(n, resid_full,'r.');
    xlabel('Echo index (n)'); ylabel('Residuals (rad)');
    legend('slope-only','slope+ripple','Location','best');

    % --- Output structure
    out = struct( ...
        'n',n, 'phi_geo',phi_geo, ...
        'slope_rad_per_echo',slope, ...
        'slope_se_rad_per_echo',slope_se, ...
        'ripple4_amp_rad',ripple_amp, ...
        'ripple4_amp_se_rad',ripple_amp_se, ...
        'ripple4_phase_rad',ripple_phase, ...
        'slope_only_rad_per_echo',slope_only, ...
        'slope_only_se_rad_per_echo',slope_only_se, ...
        'AIC_lin',AIC_lin,'AIC_full',AIC_full, ...
        'Fstat',F,'pval',pval, ...
        'fit_lin',yfit_lin,'fit_full',yfit_full, ...
        'resid_lin',resid_lin,'resid_full',resid_full);
end
```

CRediT authorship contribution statement

Sophia N. Fricke: Writing – review & editing, Writing – original draft, Visualization, Software, Methodology, Investigation, Formal analysis, Data curation, Conceptualization. **Jeffrey A. Reimer:** Writing – review & editing, Visualization, Validation, Supervision, Resources, Project administration.

Declaration of competing interest

The authors declare that they have no known competing financial interests or personal relationships that could have appeared to influence the work reported in this paper.

Acknowledgements

S.N.F. gratefully acknowledges support as a Pines Magnetic Resonance Center postdoctoral fellow. We thank B. Gizatullin of Magritek for assistance with software.

Appendix A. Geometric phase for Zeeman eigenstates and coherences

Here we develop and generalize the expression for geometric phase accumulated by spin eigenstates and, more importantly for bulk NMR, by the coherences detected experimentally in terms of curvature. The following is a derivation of Eq. (8a) and (8b) in the main text, where the geometric phase of an instantaneous Zeeman eigenstate is written as $-m_s\Omega$. [31–34] We start with the Berry connection (a vector potential on parameter space) and its curvature (the corresponding field strength), translate the result into the coherence phase $\rho_{m_s m_s'}$ accessed in bulk NMR, and show how this generalizes to higher spins and multiple quantum coherences. The Berry connection defines parallel transport, curvature measures its non-integrability, the accumulated phase around a loop is the curvature flux through the enclosed surface.

First, consider a spin-½ system with instantaneous eigenstates $|+\rangle \equiv \left|m_s = +\frac{1}{2}; \widehat{\mathbf{n}}\right\rangle$ and $|-\rangle \equiv \left|m_s = -\frac{1}{2}; \widehat{\mathbf{n}}\right\rangle$, where $\widehat{\mathbf{n}}(t)$ denotes the direction of the effective field and m_s denotes the spin quantum number. In this basis, the density matrix may be written as

$$\widehat{\rho} = \begin{pmatrix} \rho_{++} & \rho_{+-} \\ \rho_{-+} & \rho_{--} \end{pmatrix}, \tag{A.1}$$

with elements $\rho_{++} = \langle + |\widehat{\rho}+\rangle$, $\rho_{+-} = \langle + |\widehat{\rho}-\rangle$, $\rho_{-+} = \langle - |\widehat{\rho}+\rangle$, and $\rho_{--} = \langle - |\widehat{\rho}-\rangle$. The detected transverse signal is proportional to the difference of the single quantum coherences ρ_{-+} and ρ_{+-}. Thus, bulk NMR is sensitive not to the absolute geometric phase of a single eigenstate, but to the relative phase accumulated between two eigenstates, encoded in the evolution of the coherence.

Using this notation, we can more generally consider a spin S in an effective field direction $\widehat{\mathbf{n}}(\theta,\varphi)$, with instantaneous eigenstates $|m_s;\widehat{\mathbf{n}}\rangle$ defined by

$$(\widehat{\mathbf{n}}\cdot\mathbf{S})|m_s;\widehat{\mathbf{n}}\rangle = m_s|m_s;\widehat{\mathbf{n}}\rangle, \tag{A.2}$$

where $m_s \in \{-S, -S+1, \ldots, S\}$. These eigenstates can be conveniently parametrized by rotating the fixed $\widehat{\mathbf{z}}$-quantized basis $|m_s\rangle \equiv |m_s;\widehat{\mathbf{z}}\rangle$ into the direction $\widehat{\mathbf{n}}$. This rotation can be introduced as an SU(2) operator in the spin-S representation

$$U(\theta,\varphi)=e^{-i\varphi S_z}\,e^{-i\theta S_y},\tag{A.3}$$

so that

$$|m_s;\widehat{\mathbf{n}}(\theta,\varphi)\rangle=U(\theta,\varphi)|m_s\rangle.\tag{A.4}$$

Any other choice of basis differs by a gauge phase $e^{i\chi(\theta,\varphi)}$, which changes the vector potential (and hence Berry connection) but not the curvature or the solid angle relation [35].

The Berry connection 1-form for the eigenstate $|m_s;\widehat{\mathbf{n}}\rangle$ is given by

$$A\equiv i\langle m_s;\widehat{\mathbf{n}}\mathbf{d}mm_s;\widehat{\mathbf{n}}\rangle=i\langle m_s|U^\dagger\mathbf{d}U|m_s\rangle,\tag{A.5}$$

where $\mathbf{d}$ is the exterior derivative on the parameter manifold (here, the Bloch sphere parametrized by θ,φ). The geometric phase around a closed loop C in parameter space is then the holonomy

$$\varphi^{\mathrm{geo}}_{m_s}(C)=\oint_C A.\tag{A.6}$$

To compute A, we evaluate $U^\dagger\mathbf{d}U$ explicitly

$$\mathbf{d}U=(\partial_\theta U)\,d\theta+(\partial_\varphi U)\,d\varphi.\tag{A.7}$$

Using Eq. (A.3), the derivative with respect to θ around the meridian yields

$$\partial_\theta U=e^{-i\varphi S_z}\left(-iS_y\right)e^{-i\theta S_y}\Rightarrow U^\dagger\partial_\theta U=e^{i\theta S_y}e^{i\varphi S_z}\,e^{-i\varphi S_z}\left(-iS_y\right)e^{-i\theta S_y}\;=\;-iS_y,\tag{A.8}$$

such that

$$i\langle m_s|U^\dagger\partial_\theta U|m_s\rangle=i\langle m_s|\left(-iS_y\right)|m_s\rangle=\langle m_s|S_y|m_s\rangle=0.\tag{A.9}$$

Next, the derivative with respect to φ around the azimuth yields

$$\partial_\varphi U=(-iS_z)\,U\Rightarrow U^\dagger\partial_\varphi U=\;-i\,U^\dagger S_zU.\tag{A.10}$$

To calculate the rotated operator $U^\dagger S_zU$, realize that the φ-rotations cancel inside $U^\dagger S_zU$, leaving

$$U^\dagger S_zU=e^{i\theta S_y}S_ze^{-i\theta S_y}\;=S_z\cos\theta+S_x\sin\theta.\tag{A.11}$$

Taking the expectation in $|m_s\rangle$, an eigenstate of S_z, gives

$$\langle m_sS_zmm_s\rangle=m_s,\tag{A.12a}$$

$$\langle m_s|S_{x,y}|m_s\rangle=0.\tag{A.12b}$$

Thus,

$$i\langle m_s|U^\dagger\partial_\varphi U|m_s\rangle=i\langle m_s|(-i)(S_z\cos\theta+S_x\sin\theta)\,|m_s\rangle=m_s\cos\theta.\tag{A.13}$$

In this gauge, then,

$$A=A_\varphi\,d\varphi,\tag{A.14a}$$

$$A_\varphi=m_s\cos\theta.\tag{A.14b}$$

From here, it appears that the connection is $m_s\cos\theta d\varphi$, whereas the standard monopole expression is typically written in terms of $(1-\cos\theta)$. The difference is purely a gauge term, since

$$m_s\cos\theta d\varphi=\;-m_s(1-\cos\theta)d\varphi+m_sd\varphi.\tag{A.15}$$

The last term, $m_s\,d\varphi\;=d(m_s\varphi)$, is locally exact, which means that it can be absorbed by a gauge transformation

$$|m_s;\widehat{\mathbf{n}}\rangle\rightarrow e^{-im_s\varphi}|m_s;\widehat{\mathbf{n}}\rangle.\tag{A.16}$$

This does not change the curvature $F\;=\mathbf{d}A$, and it only changes $\oint A$ by integer multiples of 2π when the loop winds around the φ coordinate (i.e., in the xy plane).

Here the physically meaningful object is the curvature (field strength), and the holonomy is most easily computed using a gauge that is nonsingular on the surface chosen by the pulse sequence [35]. To this end, we choose the conventional gauge potential

$$A=\;-m_s(1-\cos\theta)d\varphi,\tag{A.17}$$

which is smooth everywhere except at one pole (i.e., a Dirac string) [35]. This is the direct analogue of a vector potential whose curl produces a monopole field. Taking the exterior derivative gives the curvature 2-form

$$F\equiv\mathbf{d}A=\mathbf{d}(-m_s(1-\cos\theta)d\varphi\,)=\;-m_s\sin\theta d\theta\wedge d\varphi.\tag{A.18}$$

Here, $d\theta\wedge d\varphi$ denotes the antisymmetric wedge product of the coordinate 1-forms, $d\theta\wedge d\varphi\;=\;-\;d\varphi\wedge d\theta$, which ensures that the 2-form F

transforms correctly under reparametrization of the surface; the scalar shorthand $\sin\theta d\theta d\varphi$ used in Eqs. (A.20)–(A.21) follows once an orientation is fixed. Importantly, this curvature is gauge-invariant because it is independent of the particular choice of phase convention for $|m_s;\hat{\mathbf{n}}\rangle$; it acts as the Faraday tensor on the parameter manifold [13].

Applying Stokes' theorem on the sphere relates this curvature 2-form to the geometric phase. For a closed path C traced by $\hat{\mathbf{n}}(t)$, let Σ denote any surface on the sphere whose boundary is C, such that $\partial\Sigma = C$. (Then)

$$\varphi_{m_s}^{\text{geo}}(C) = \oint_C A = \iint_\Sigma F. \tag{A.19}$$

Using the expression for F in Eq. (A.18),

$$\varphi_{m_s}^{\text{geo}}(C) = \iint_\Sigma (-m_s \sin\theta d\theta\, d\varphi) = -m_s \iint_\Sigma \sin\theta d\theta\, d\varphi. \tag{A.20}$$

Happily, this remaining integral is exactly the oriented solid angle Ω subtended by Σ on the unit sphere:

$$\Omega(\Sigma) = \iint_\Sigma \sin\theta d\theta\, d\varphi. \tag{A.21}$$

Therefore, we have derived the expression in Eq. (8a):

$$\varphi_{\text{geo}} = -m_s\Omega. \tag{A.22}$$

This relation tells us that geometric phase is curvature flux, with m_s acting as an effective monopole charge coupling to the curvature, and the sign fixed by the convention adopted above.

However, bulk NMR does not measure this global eigenket phase; instead, it measures phases of coherences. To connect directly to what is detected in the framework developed here, consider a density matrix element in the instantaneous eigenbasis,

$$\rho_{m_s m_s'} \equiv \langle m_s;\hat{\mathbf{n}}|\hat{\rho}|m_s';\hat{\mathbf{n}}\rangle. \tag{A.23}$$

Under cyclic adiabatic evolution, the eigenkets transform as $|m_s;\hat{\mathbf{n}}\rangle \rightarrow e^{i\varphi_{m_s}}|m_s;\hat{\mathbf{n}}\rangle$, where φ_{m_s} includes both dynamic and geometric contributions. The density matrix transforms as $\hat{\rho} \rightarrow U\rho U^\dagger$, which indicates the off-diagonal element transforms as

$$\rho_{m_s m_s'} \rightarrow e^{i\varphi_{m_s}}\rho_{m_s m_s'} e^{-i\varphi_{m_s'}} = e^{i\left(\varphi_{m_s} - \varphi_{m_s'}\right)}\rho_{m_s m_s'}. \tag{A.24}$$

Hence, the coherence phase is inherently a difference of eigenstate phases. Isolating the geometric part gives the expression in Eq. (8b):

$$\varphi_{m_s m_s'}^{\text{geo}} = \varphi_{m_s}^{\text{geo}} - \varphi_{m_s'}^{\text{geo}} = (-m_s\Omega) - (-m_s'\Omega) = -(m_s - m_s')\Omega. \tag{A.25}$$

Defining the coherence order $q \equiv m_s - m_s'$ allows the experimentally relevant geometric phase to be written more compactly as

$$\varphi_{m_s m_s'}^{\text{geo}} = -q\Omega. \tag{A.26}$$

Thus, for spin-½, each eigenstate accumulates geometric phase as $\pm\Omega/2$, but the detected single-quantum coherence connecting $m_s = +1/2$ and $m_s' = -1/2$ has $q = 1$, so the coherence accumulates geometric phase as $-\Omega$. For an equatorial loop with $\Omega = 2\pi$, the coherence geometric phase per loop is -2π, consistent with what is extracted from the interferometric echo train-derived slopes in the main text.

The same derivation applies unchanged for higher spins. The only input is that $\langle m_s|S_z|m_s\rangle = m_s$ and $\langle m_s|S_{x,y}|m_s\rangle = 0$, so the curvature remains proportional to m_s, and coherences always carry the difference $q \equiv m_s - m_s'$. For spin-1 ($m_s \in \{-1, 0, +1\}$), eigenstate geometric phases are $\varphi_{+1} = -\Omega$, $\gamma_0 = 0$, $\varphi_{-1} = +\Omega$. Single-quantum coherences ($q = 1$) acquire geometric phase equivalent to $-\Omega$, while double-quantum coherences ($q = 2$) acquire -2Ω. For spin-$\frac{3}{2}$ ($m_s \in \left\{-\frac{3}{2}, -\frac{1}{2}, +\frac{1}{2}, +\frac{3}{2}\right\}$), the eigenstate phases are $\varphi_{m_s} = -m_s\Omega$ (i.e., $\pm\frac{3}{2}\Omega$ and $\pm\frac{1}{2}\Omega$), while single-, double-, and triple-quantum coherences acquire geometric phase proportional to $-\Omega$, -2Ω, and -3Ω, respectively. In general, for any spin S, the geometric phase of a coherence is always $-q\Omega$, with q the coherence order. This is the natural geometric observable for bulk NMR interferometry, where coherences are the measured objects.

Data availability

The codes supporting this article have been included and data are available upon reasonable request.

References

[1] M.V. Berry, Quantal phase factors accompanying adiabatic changes, Proc. R. Soc. Lond. A. Math. Phys. Sci. 392 (1984) 45–57, https://doi.org/10.1098/rspa.1984.0023.

[2] Y. Aharonov, J. Anandan, Phase change during a cyclic quantum evolution, Phys. Rev. Lett. 58 (1987) 1593–1596, https://doi.org/10.1103/PhysRevLett.58.1593.

[3] E. Cohen, H. Larocque, F. Bouchard, F. Nejadsattari, Y. Gefen, E. Karimi, Geometric phase from Aharonov–Bohm to Pancharatnam–Berry and beyond, Nat. Rev. Phys. 1 (2019) 437–449, https://doi.org/10.1038/s42254-019-0071-1.

[4] J.W. Zwanziger, M. Koenig, A. Pines, Berry's phase, Annu. Rev. Phys. Chem. 41 (1990) 601–646, https://doi.org/10.1146/annurev.pc.41.100190.003125.

[5] A.W. Overhauser, R. Colella, Experimental test of gravitationally induced quantum interference, Phys. Rev. Lett. 33 (1974) 1237–1239, https://doi.org/10.1103/PhysRevLett.33.1237.

[6] H. Rauch, A. Zeilinger, G. Badurek, A. Wilfing, W. Bauspiess, U. Bonse, Verification of coherent spinor rotation of fermions, Phys. Lett. A 54 (1975) 425–427, https://doi.org/10.1016/0375-9601(75)90798-7.

[7] M.E. Stoll, A.J. Vega, R.W. Vaughan, Explicit demonstration of spinor character for a spin-½ nucleus via NMR interferometry, Phys. Rev. A (Coll Park) 16 (1977) 1521–1524, https://doi.org/10.1103/PhysRevA.16.1521.

[8] D. Suter, A. Pines, M. Mehring, Indirect phase detection of NMR spinor transitions, Phys. Rev. Lett. 57 (1986) 242–244, https://doi.org/10.1103/PhysRevLett.57.242.

[9] C. Bengs, M. Sabba, M.H. Levitt, The Aharonov–Anandan phase and geometric double-quantum excitation in strongly coupled nuclear spin pairs, J. Chem. Phys. 158 (2023), https://doi.org/10.1063/5.0138146.

[10] U.D. Heramun, M. Sabba, C. Bengs, G.A.I. Moustafa, M.H. Levitt, Singlet NMR in a case of high molecular symmetry, J. Chem. Phys. 163 (2025), https://doi.org/10.1063/5.0286843.

[11] R. Tycko, Adiabatic rotational Splittings and Berry's phase in nuclear quadrupole resonance, Phys. Rev. Lett. 58 (1987) 2281–2284, https://doi.org/10.1103/PhysRevLett.58.2281.

[12] L. Emsley, A. Pines, Lectures on pulsed NMR, in: Proceedings of the International School of Physics, Enrico Fermi, 2nd ed., Societa Italiana di Fisica, 2023.
[13] C.W. Misner, K.S. Thorne, J.A. Wheeler, Gravitation, W. H. Freeman, San Francisco, 1973.
[14] E. Lippert, J.D. Macomber, Dynamics during Spectroscopic Transitions, Springer Berlin Heidelberg, Berlin, Heidelberg, 1995, https://doi.org/10.1007/978-3-642-79407-0.
[15] J.I. Steinfeld, Molecules and Radiation : An Introduction to Modern Molecular Spectroscopy, Dover Publications, 2012.
[16] L.P. Kadanoff, G. Baym, Quantum statistical mechanics, CRC Press, 2018, https://doi.org/10.1201/9780429493218.
[17] H.J.W. Haug, A.-P. Jauho, Quantum Kinetics in Transport and Optics of Semiconductors, Springer Berlin Heidelberg, Berlin, Heidelberg, 2008, https://doi.org/10.1007/978-3-540-73564-9.
[18] J. Rammer, Classical statistical dynamics, in: Quantum Field Theory of Non-Equilibrium States, Cambridge University Press, 2007, pp. 449–502, https://doi.org/10.1017/CBO9780511618956.013.
[19] Y. Meir, N.S. Wingreen, Landauer formula for the current through an interacting electron region, Phys. Rev. Lett. 68 (1992) 2512–2515, https://doi.org/10.1103/PhysRevLett.68.2512.
[20] C. Slichter, Principles of Magnetic Resonance, 3rd edition, Springer, 1990.
[21] A. Abragam, The Principles of Nuclear Magnetism, Clarendon Press, 1983.
[22] I. Kuprov, Spin, springer international publishing, Cham, 2023, https://doi.org/10.1007/978-3-031-05607-9.
[23] M.H. Levitt, Spin Dynamics: Basics of Nuclear Magnetic Resonance, 2nd edition, Wiley, 2008.
[24] H.Y. Carr, Steady-state free precession in nuclear magnetic resonance, Phys. Rev. 112 (1958) 1693–1701, https://doi.org/10.1103/PhysRev.112.1693.
[25] H.Y. Carr, E.M. Purcell, Effects of diffusion on free precession in nuclear magnetic resonance experiments, Phys. Rev. 94 (1954) 630–638, https://doi.org/10.1103/PhysRev.94.630.
[26] S. Meiboom, D. Gill, Modified spin-Echo method for measuring nuclear relaxation times, Rev. Sci. Instrum. 29 (1958) 688–691, https://doi.org/10.1063/1.1716296.
[27] S. Weinberg, The Quantum Theory of Fields, Cambridge University Press, 2000, https://doi.org/10.1017/CBO9781139644198.
[28] S.N. Fricke, V. Witherspoon, J. Demarteau, B.A. Helms, J.A. Reimer, Mapping structures and dynamics with frequency-correlated diffusion exchange, Sci. Adv. 11 (2025), https://doi.org/10.1126/sciadv.ady8380.
[29] S.N. Fricke, M. Salgado, S. Haber, J. Demarteau, M. Hua, A.-Y. Song, B.A. Helms, J. A. Reimer, Diffusion power spectra as a window into dynamic materials architecture, Sci. Adv. 11 (2025), https://doi.org/10.1126/sciadv.adt6144.
[30] P.T. Callaghan, Translational Dynamics and Magnetic Resonance, Oxford University Press, 2011, https://doi.org/10.1093/acprof:oso/9780199556984.001.0001.
[31] Alfred. Shapere, Frank. Wilczek, Geometric Phases in Physics, World Scientific, 1989.
[32] Ramamurti. Shankar, Principles of Quantum Mechanics, Springer, 2014.
[33] M. Stone, Born-Oppenheimer approximation and the origin of Wess-Zumino terms: some quantum-mechanical examples, Phys. Rev. D 33 (1986) 1191–1194, https://doi.org/10.1103/PhysRevD.33.1191.
[34] D. Suter, K.T. Mueller, A. Pines, Study of the Aharonov-Anandan quantum phase by NMR interferometry, Phys. Rev. Lett. 60 (1988) 1218–1220, https://doi.org/10.1103/PhysRevLett.60.1218.
[35] L.H. Ryder, Quantum Field Theory, Cambridge University Press, 2019.
[36] R.T. Branca, G. Galiana, W.S. Warren, Signal enhancement in CRAZED experiments, J. Magn. Reson. 187 (2007) 38–43, https://doi.org/10.1016/j.jmr.2007.02.017.
[37] C. Ramanathan, R. Bowtell, Dynamics of the nuclear magnetic resonance COSY-revamped by asymmetric z -gradients (CRAZED) experiment, J. Chem. Phys. 114 (2001) 10854–10859, https://doi.org/10.1063/1.1375026.
[38] P.T. Callaghan, J. Stepišnik, Frequency-domain analysis of spin motion using modulated-gradient NMR, J. Magn. Reson. A 117 (1995) 118–122, https://doi.org/10.1006/jmra.1995.9959.
[39] G. Eidmann, R. Savelsberg, P. Blümler, B. Blümich, The NMR MOUSE, a Mobile universal surface explorer, J. Magn. Reson. A 122 (1996) 104–109, https://doi.org/10.1006/jmra.1996.0185.
[40] B. Blümich, J. Anders, When the MOUSE leaves the house, magnetic, Resonance 2 (2021) 149–160, https://doi.org/10.5194/mr-2-149-2021.